

Quantitative Diffusion Imaging With Steady-State Free Precession

Sean C.L. Deoni,^{1,2} Terry M. Peters,^{1,2,3} and Brian K. Rutt^{1,2,3}

The addition of a single, unbalanced diffusion gradient to the steady-state free precession (SSFP) imaging sequence sensitizes the resulting signal to free diffusion. Unfortunately, the confounding influence of both longitudinal (T_1) and transverse (T_2) relaxation on the diffusion-weighted SSFP (dwSSFP) signal has made it difficult to quantitatively determine the apparent diffusion coefficient (ADC). Here, a multistep method in which the T_1 , T_2 , and spin density (M_o) constants are first determined using a rapid mapping technique described previously is presented. Quantitative ADC can then be determined through a novel inversion of the appropriate signal model. The accuracy and precision of our proposed method (which we term DESPOD) was determined by comparing resulting ADC values from phantoms to those calculated from traditional diffusion-weighted echo planar imaging (dwEPI) images. Error within the DESPOD-derived ADC maps was found to be less than 3%, with good precision over a biologically relevant range of ADC values. *Magn Reson Med* 51:428–433, 2004. © 2004 Wiley-Liss, Inc.

Key words: apparent diffusion coefficient; steady-state free precession; diffusion imaging; rapid volumetric imaging

Diffusion-weighted imaging (DWI) has been shown to provide diagnostically useful information about the brain following stroke (1,2), as well as prostate and other cancers (3,4). Increasingly, the ability to measure the apparent diffusion coefficient (ADC) with high resolution, precision, and accuracy has become an important addition to qualitative DWI. Quantitatively determining the ADC along at least six encoding directions makes it possible to describe the local diffusion tensor and is useful in the study of various central nervous system disorders (5).

When a single, unbalanced diffusion gradient is added to the steady-state free precession (SSFP) imaging sequence, the resulting signal is strongly sensitized to intravoxel incoherent motion and free molecular diffusion (6). The diffusion sensitivity of diffusion-weighted SSFP (dwSSFP) has previously been investigated by several authors (6–10), starting with Kaiser et al. (6), who examined the effect of adding a constant unbalanced diffusion gra-

dient to the SSFP sequence in NMR spectroscopy. Wu and Buxton (7) extended this analysis to the pulsed gradients more commonly employed in imaging applications. By solving the Bloch equations using a Fourier series approximation, Wu and Buxton derived a general equation for the signal immediately following and preceding the RF pulse (S^+ and S^- , respectively) with the addition of a diffusion gradient of strength G and duration δ . LeBihan et al. (8) derived an alternative derivation of S^+ and S^- by modifying the diffusion-free Bloch equations and treating the diffusion attenuation as an effective T_2 shortening and looking specifically at the case where 90° flip angles are used. Despite the ability to characterize the S^+ and S^- signals, dwSSFP has not been presented as a means of quantitatively determining ADC due to the confounding influence of longitudinal (T_1) and transverse (T_2) relaxation and spin density (M_o).

In this article we present novel inversions of the Wu and Buxton and LeBihan signal equations allowing ADC to be determined with high accuracy and precision from a single dwSSFP image, provided T_1 , T_2 , and M_o are known. To determine these latter variables, we propose the use of the DESPOT1 and DESPOT2 methods previously described in Ref. 11. Here, T_1 is first determined through the use of DESPOT1 and involves the collection of two or more spoiled gradient recalled echo (SPGR) images at different flip angles. T_2 and M_o are then calculated from two or more fully refocused SSFP images also acquired at different flip angles (DESPOT2). In keeping with the naming convention of DESPOT1 and DESPOT2, we have named our new diffusion mapping method DESPOD (driven equilibrium single pulse observation of diffusion).

THEORY

Wu and Buxton Model

The addition of a single gradient pulse of strength G and duration δ , immediately following the RF pulse of the fully balanced SSFP sequence, acts to spoil the S^+ signal and modifies the measured S^- signal by introducing a diffusion dependence. This is the same signal measured in CE-FAST (10) and time-reversed FISP (PSIF) (12) imaging sequences where all imaging gradients are fully balanced around the echo. The equation for this signal in the presence of diffusion, $S_{WuBuxton}^-$, is given by:

$$S_{WuBuxton}^- = \frac{-M_o(1 - E_1)(F - E_2A_1A_2^{-2/3})E_2A_2^{1/3}\sin \alpha}{r - Fs}, \quad [1a]$$

where:

$$r = 1 - E_1\cos \alpha + E_2^2A_1A_2^{-1/3}(\cos \alpha - E_1), \quad [1b]$$

¹Imaging Research Laboratories, Robarts Research Institute, London, Ontario, Canada.

²Department of Medical Biophysics, University of Western Ontario, London, Ontario, Canada.

³Department of Diagnostic Radiology and Nuclear Medicine, University of Western Ontario, London, Ontario, Canada.

Grant sponsor: Canadian Institutes for Health Research; Grant numbers: MT-11540; GR-14973; Grant sponsors: Canadian Foundation for Innovation, the University of Western Ontario, and General Electric Medical Systems (Milwaukee, WI).

*Correspondence to: Brian K. Rutt, Imaging Research Laboratories, Robarts Research Institute, P.O. Box 5015, 100 Perth Drive, London, Ontario N6A 5K8, Canada. E-mail: brutt@imaging.robarts.ca

Received 15 April 2003; revised 30 September 2003; accepted 2 October 2003.

DOI 10.1002/mrm.10708

Published online in Wiley InterScience (www.interscience.wiley.com).

© 2004 Wiley-Liss, Inc.

$$s = E_2 A_1 A_2^{4/3} (1 - E_1 \cos \alpha) + E_2 A_2^{1/3} (\cos \alpha - E_1), \quad [1c]$$

$$K = \frac{1 - E_1 A_1 \cos \alpha - E_2^2 A_1^2 A_2^{2/3} (E_1 A_1 - \cos \alpha)}{E_2 A_1 A_2^{4/3} (\cos \alpha + 1) (1 - E_1 A_1)}, \quad [1d]$$

$$F = K - \sqrt{K^2 - A_2^{-2}}, \quad [1e]$$

$$A_1 = \exp(-(\gamma G \delta)^2 TR \cdot ADC), \quad [1f]$$

$$A_2 = \exp(-(\gamma G \delta)^2 \delta \cdot ADC), \quad [1g]$$

$$E_1 = \exp(-TR/T_1), \quad [1h]$$

$$E_2 = \exp(-TR/T_2). \quad [1i]$$

In the above equations, TR is the repetition time and α is the flip angle.

In the limit of $\delta \ll TR$, $A_2 \approx 1$, and A_1 (redefined as A for simplicity) can be determined in the following manner. First, letting:

$$\beta = \frac{-S_{WuBuxton}^-}{M_o(1 - E_1)E_2 \sin \alpha}, \quad [2]$$

we simplify Eq. [1] to:

$$\beta = \frac{F - E_2 A}{r - F s}. \quad [3]$$

Simplifying Eq. [3] as outlined in the Appendix yields the expression:

$$aA^2 + bA + c = \left(\frac{gA^3 + hA^2 + iA + 1}{jA^2 + kA} \right) (dA^2 + eA + f), \quad [4]$$

where a,b,c,d,e,f,g,h,i,j, and k are as defined in the Appendix. Simplifying gives a final fifth degree polynomial in A :

$$mA^5 + nA^4 + oA^3 + pA^2 + qA + f = 0, \quad [5]$$

where $m = dg$, $n = (eg + hd - aj)$, $o = (gf + eh + id - ak - bj)$, $p = (hf + ie + d - bk - jc)$ and $q = (if + e - kc)$. A is the first real positive root of this polynomial and the apparent diffusion coefficient, ADC, can be calculated as:

$$ADC = -\ln(A)/b_{WuBuxton}. \quad [6]$$

Here, $b_{WuBuxton} = (\gamma G \delta)^2 TR$, as defined by Wu and Buxton (7), is indicative of the diffusion weighting applied.

In the preceding analysis we assumed that $\delta \ll TR$. If the diffusion-encoding gradient is applied for most of the TR interval this assumption is no longer appropriate and instead we assume $\delta \approx TR$ and, therefore, $A_2 \approx A_1 \approx A$. Under this condition, we rewrite $S_{WuBuxton}^-$ as:

$$S_{WuBuxton}^- = \frac{-M_o(1 - E_1)(F' - E_2 A^{1/3})E_2 A^{1/3} \sin \alpha}{r' - F' s'}, \quad [7a]$$

where:

$$r' = 1 - E_1 \cos \alpha + E_2^2 A^{2/3} (\cos \alpha - E_1), \quad [7b]$$

$$s' = E_2 A^{7/3} (1 - E_1 \cos \alpha) + E_2 A^{1/3} (\cos \alpha - E_1). \quad [7c]$$

$$K' = \frac{1 - E_1 A \cos \alpha - E_2^2 A^{8/3} (E_1 A - \cos \alpha)}{E_2 A^{7/3} (\cos \alpha + 1) (1 - E_1 A)}, \quad [7d]$$

$$F' = K' - \sqrt{K'^2 - A^{-2}}. \quad [7e]$$

As with Eq. [1], we can solve for A by reducing Eq. [7] to a high order (21 degree) polynomial. Unfortunately, this polynomial is extremely sensitive to noise in the measured signal intensity. A less sensitive method of determining A is by searching for the zero-crossing of the function $y(A)$, where

$$y(A) = \beta'(r' - F' s') - (F' - E_2 A^{1/3}) A^{1/3} \quad [8]$$

and

$$\beta' = \frac{-S_{WuBuxton}^-}{M_o(1 - E_1)E_2 \sin \alpha}. \quad [9]$$

To find the zero-crossing quickly and robustly we use a variant of the rapid T_1 mapping algorithm described by Gong and Hornak (13). The algorithm proceeds in the following manner. $y(A)$ is evaluated at two initial points, $x_1 = 0.00$ and $x_2 = 1.00$. The x-intercept (ϵ) of the line connecting $y(A = x_1)$ and $y(A = x_2)$ is calculated and $y(A = \epsilon)$ is evaluated. If $|y(A = \epsilon)| < 0.0001$, ϵ is taken as the solution for A . Otherwise, $x_1 = 0.00$ is redefined as $x_1 = \epsilon$ and the algorithm repeats itself.

LeBihan Model

LeBihan (8) presented a derivation of the dwSSFP S^- signal ($S_{LeBihan}^-$) as:

$$S_{LeBihan}^- = \frac{M_o \sin \alpha}{(1 + \cos \alpha)} \left\{ 1 - (1 - E_1 \cos \alpha) \sqrt{\frac{1 - E_2^2 A^2}{t}} \right\}, \quad [10]$$

where $t = 1 - E_1^2 E_2^2 A^2 - 2E_1 \cos \alpha + E_1^2 \cos^2 \alpha - E_2^2 A^2 \cos^2 \alpha$ and $A = \exp(-(\gamma G \delta)^2 (TR - 2\delta/3) \cdot ADC)$. An analytical solution for A can also be found in this case. Letting $\chi = S_{LeBihan}^- (1 + \cos \alpha) / (M_o \sin \alpha)$ and $\kappa = \chi^2 - 2\chi + 1 / (1 - E_1 \cos \alpha)^2$, and substituting these results into Eq. [10] gives:

$$\kappa t = 1 - E_2^2 A^2. \quad [11]$$

Expanding Eq. [11] and collecting the A^2 terms gives:

$$\begin{aligned} \kappa - 2\kappa E_1 \cos \alpha + \kappa E_1^2 \cos^2 \alpha - 1 \\ = A^2 (\kappa E_1^2 E_2^2 - 2\kappa E_1 E_2^2 \cos \alpha + \kappa E_2^2 \cos^2 \alpha - E_2^2) \end{aligned} \quad [12]$$

which yields:

$$A = \sqrt{\frac{\kappa - 2\kappa E_1 \cos \alpha + \kappa E_1^2 \cos^2 \alpha - 1}{\kappa E_1^2 E_2^2 - 2\kappa E_1 E_2^2 \cos \alpha + \kappa E_2^2 \cos^2 \alpha - E_2^2}}. \quad [13]$$

In the specific case where $\alpha = 90^\circ$, we can simplify Eq. [13] to:

$$A = \frac{1}{E_2} \sqrt{\frac{\kappa - 1}{\kappa E_1^2 - 1}}. \quad [14]$$

ADC is calculated from either Eq. [13] or [14] as:

$$ADC = -\ln(A)/b_{LeBihan}. \quad [15]$$

Here, $b_{LeBihan} = (\gamma G \delta)^2 (TR - 2\delta/3)$ is defined slightly differently than in the Wu-Buxton derivation.

It is clear, then, that the ADC may be extracted from either the Wu and Buxton (under both $A_2 \approx 1$ or $A_2 \approx A$ assumptions) or LeBihan signal equations, provided T_1 , T_2 , and M_o are known. Given the dissimilarity of the models and the different assumptions made in each, experimental validation is necessary to determine which model provides a more accurate and reliable fit to the experimental data.

MATERIALS AND METHODS

To examine the validity of the Wu and Buxton and LeBihan signal equations, we compared the theoretical models with experimentally acquired data. DESPOT1, DESPOT2, and multiangle DESPOD data were acquired of a spherical (10 cm diameter) water-filled phantom with a 25 cm² field of view (FOV), 256 × 256 × 100 matrix with 1 mm slice thickness (ST). Sequence specific parameters are listed below. DESPOT1, DESPOT2, and DESPOD data were acquired using variants of a 3D SSFP imaging sequence in which the transverse magnetization was either spoiled (DESPOT1), fully refocused, i.e., fully balanced SSFP (DESPOT2), or with an additional unbalanced gradient (DESPOD). For all sequences, phase-alternated RF pulses were used. All images were acquired on a clinical 1.5 T CV/i system (GE Medical Systems, Milwaukee, WI) using a quadrature birdcage head coil.

DESPOT1: Flip angles (FA) = 3° and 12°, echo time (TE) = 1.1 ms, repetition time (TR) = 3.8 ms, number of excitations (NEX) = 1, imaging time = 6:29.

DESPOT2: FA = 20° and 80°, TE = 1.8 ms, TR = 3.7 ms, NEX = 1, imaging time = 6:18.

DESPOD: FA: from 9° to 90° in 9° increments, diffusion gradient strength (G) = 20 mT × m⁻¹, diffusion gradient area (GA) = (100, 120, 140, 160, 180, 200, 220, 240, 260, 280, 300, 350, 400, and 450) mT × ms × m⁻¹, corresponding to b-values of 19, 28, 39, 51, 64, 79, 96, 114, 133, 155, 178, 242, 316 and 400 s × mm⁻² (using the Wu-Buxton definition). TR was held constant at 28.6 ms, TE varied from 8.6 ms to 26.2 ms as GA was incremented. Half Fourier (i.e., NEX = 0.5) imaging was employed to decrease the scan time by approximately one-half to 61 min for all 10 angles at each b-value. The 10 different angles were acquired only to validate the theoretical signal equa-

tions; in general, only a single angle is needed to determine the ADC using DESPOD.

Data acquired with a conventional 2D diffusion-weighted echo planar imaging (dwEPI) sequence with diffusion encoding along all three axes were used to determine the gold standard ADC value of the water phantom. The dwEPI image was acquired with a 25 cm² FOV and 128 × 128 matrix, 10 mm ST, TE = 61.7 ms, TR = 5,000 ms, NEX = 9, and b-value of 600 s × mm⁻². The resulting T_1 , T_2 , M_o , and the gold standard ADC values were substituted into Eqs. [1], [7], and [10] to generate theoretical signal curves for each model. These curves were then compared with the experimental DESPOD data acquired at multiple angles.

To evaluate the accuracy and precision of the method, voxel-wise ADC maps of five spherical phantoms containing corn oil, acetone, water, and 25% and 50% glycerol solutions were calculated. DESPOT1 and DESPOT2 data were acquired from the phantoms using the parameters listed above. DESPOD data were acquired with a 25 cm² FOV, 256 × 256 × 100 matrix, 1 mm ST, with $G = 20$ mT × m⁻¹, diffusion gradient area $GA = 250$ mT × ms × m⁻¹ (corresponding to a b-value of 117 s × mm⁻²), TE = 15.1 ms, TR = 17.8 ms, NEX = 1, and FA = 90°. Total imaging time for the combined DESPOT1, DESPOT2, and DESPOD data was 20 min for each phantom. Gold standard ADC values for each phantom were calculated from dwEPI data acquired with the parameters listed above.

ADC maps were calculated using the inverted Wu-Buxton (with both the $A_2 \approx 1$ and $A_2 \approx A$ assumptions) and LeBihan signal equations. An iterative Newton's method approach was used to solve for A from the fifth degree polynomial (Eq. [5]), starting with an initial seed value of 0.3 and repeating the algorithm until the difference between successive iterations was less than 0.0001. The modified Gong-Hornak algorithm was used to solve for A from Eq. [8]. Total postprocessing time for the 3D maps was less than 20 sec for the LeBihan estimates and ~1 min for the Wu-Buxton ADC estimates using an Athlon 1.8 GHz PC.

RESULTS

Comparison of the theoretical signal models with the experimental data is shown in Fig. 1. It is clear that the Wu-Buxton model (using either the $A_2 \approx 1$ or $A_2 \approx A$ assumption) provides a closer approximation to the experimental data than the LeBihan model. Of the two variants of the Wu-Buxton model, we can see that at low b-values (i.e., < 20 s × mm⁻², Fig. 1a), both models perform equally well. At higher b-values, however, the $A_2 \approx A$ assumption more closely resembles the collected data, but only a small difference is seen compared with the $A_2 \approx 1$ assumption. Although the LeBihan model shows a considerable deviation from the experimental data over the low flip angle range, the model does agree well at flip angles greater than 80°. The diffusion attenuation observed in dwSSFP is a result of cumulative diffusion encoding over multiple TR intervals, given that the measured signal is comprised of echoes from multiple pathways (6). The LeBihan model does not accurately account for the diffusion effect on

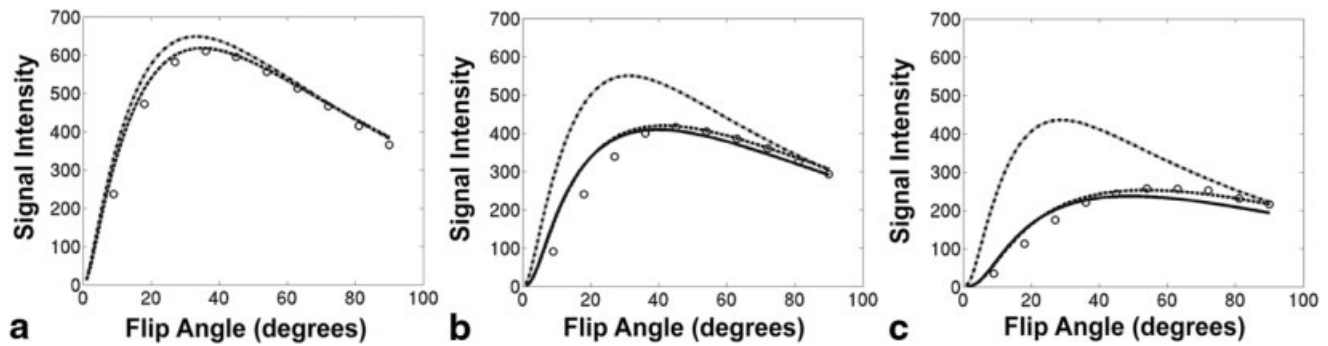


FIG. 1. Water phantom signal intensity vs. flip angle comparison of experimental data (circles) and the theoretical models of Wu and Buxton with the $A_2 \approx 1$ assumption (solid line), Wu and Buxton with the $A_2 \approx A_1$ assumption (dashed line) and LeBihan (dash-dot line) for a series of dwSSFP images over a range of diffusion gradient areas: (a) 60, (b) 160, and (c) 260 $\text{mT} \times \text{ms} \times \text{m}^{-1}$ with constant TR . For small gradient areas all models tend to approximate the experimental data well. For large diffusion gradient areas, the Wu and Buxton models provide better approximations over all flip angles with the $A_2 \approx A_1$ assumption providing a closer match. Signal intensity values are shown in arbitrary units.

these multiple pathways and this is likely the reason for the disagreement between model and experiment.

Of interest in Fig. 1 is the similarity of the Wu-Buxton signal curves with either $A_2 \approx 1$ or $A_2 \approx A$. This result suggests a general insensitivity of the model to the A_2 term. It is reasonable to believe that since the diffusion effect accumulates over multiple TR intervals, the diffusion gradient area plays the dominant role in the signal attenuation with the shape of the gradient having far less importance. Thus, for the same b-value, short or long gradient pulses of equal area produce approximately the same net signal attenuation.

Comparison of dwEPI (gold standard) and DESPOD-derived ADC values corresponding to the corn oil, acetone, water, and 25% and 50% glycerol solutions phantoms are shown in Fig. 2. Good agreement is observed between the Wu-Buxton estimates and gold standard values, particularly within the biologically relevant region ($0.42\text{--}1.0 \times 10^{-3} \text{ mm}^2 \times \text{s}^{-1}$). Variance within the estimates is lowest in the measurements calculated using the model with the $A_2 \approx A$ assumption and greatest in those calculated with the LeBihan model. Average ADC-to-noise (average ADC value divided by the stan-

dard deviation) for the three models ($A_2 \approx A$, $A_2 \approx 1$, LeBihan) were 18.5, 8.6, and 6.4, respectively. The low ADC-to-noise value of the $A_2 \approx 1$ estimates is primarily due to the relatively large variance observed in the acetone measurement. Mean error between the $A_2 \approx A$, $A_2 \approx 1$ and LeBihan and the dwEPI measurements was 2.4%, 4.3%, and 13.5%, respectively, excluding the corn oil, which has an extremely low ADC ($0.01 \times 10^{-3} \text{ mm}^2 \times \text{s}^{-1}$). Therefore, while all three models may be used to extract the ADC from a dwSSFP image, provided appropriate angles are used, the Wu-Buxton model (with $A_2 \approx A$) provides the highest precision and accuracy.

To ensure the increased variance observed in the $A_2 \approx 1$ estimates compared to the $A_2 \approx A_1$ estimates was not a result of the different root finding algorithms used, the $A_2 \approx 1$ values were recalculated using the modified Gong-Hornak algorithm, which we found to be less sensitive to noise in the $A_2 \approx A_1$ case. No significant change in the variance was observed, suggesting that the decreased precision of these estimates results from the $A_2 \approx 1$ assumption and is not a by-product of the root finding algorithm used.

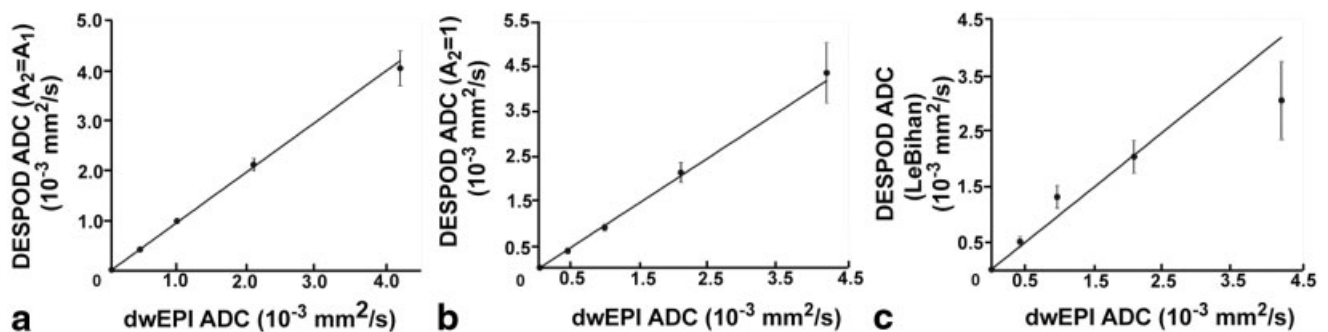


FIG. 2. Comparison of ADC values for corn oil, acetone, water, and 25% and 50% glycerol solutions calculated using dwEPI and DESPOD using the Wu-Buxton model with (a) $A_2 \approx A_1$, (b) $A_2 \approx 1$, and (c) LeBihan model. DESPOD data was acquired with a b-value of $117 \text{ s} \times \text{mm}^{-2}$ and flip angle = 90° . dwEPI data were acquired with a b-value of $600 \text{ s} \times \text{mm}^{-2}$. The line corresponds to the line of unity, the points represent the average value of a 121×121 voxel region of interest centered in the image, and the error bars represent the standard deviation of the values within the region of interest.

DISCUSSION AND CONCLUSIONS

The experimental findings presented in the preceding sections illustrate the potential of the DESPOD method. The method permits measurement of T_1 , T_2 , M_0 , and ADC in a 3D volume ($256 \times 256 \times 100$ matrix) in ~ 20 min with less than 3% error in ADC (relative to values reported by dwEPI) for biologically relevant ADC values between 0.4×10^{-3} and $5.0 \times 10^{-3} \text{ mm}^2 \times \text{s}^{-1}$.

In our proposed approach, the ADC is determined from a single dwSSFP image using previously calculated T_1 , T_2 , and M_0 values. Error in any of the T_1 , T_2 , or M_0 estimates will therefore result in error in the calculated ADC value. While an in-depth investigation of error propagation is beyond the scope of this article, the primary source of error in the T_1 , T_2 , and M_0 estimates is imprecise knowledge of the flip angles used in the DESPOT1 and DESPOT2 methods. Errors in the flip angle arise from B_1 field inhomogeneities and slice profile errors. Slice profile errors were minimized in our case through the 3D implementation of the sequence, particularly within the center portion of the 3D slab, which are excited by carefully designed SLR pulses. Patient-induced B_1 inhomogeneities are more difficult to correct, however, as noted in Ref. 11, we found that these effects did not appear to present a significant source of error at 1.5 T.

To briefly address this issue, we performed a simulation to examine the impact of error in the T_1 , T_2 , and M_0 estimates on ADC precision. For a baseline, ADC values were first calculated assuming perfect knowledge of T_1 , T_2 , and M_0 and Gaussian distributed noise added only to the dwSSFP signal. Three cases were then examined in which noise was added to the dwSSFP signal as well as to the T_1 , T_2 , and M_0 estimates individually. A final case was also included in which noise was added to the dwSSFP signal and all of T_1 , T_2 , and M_0 . Standard deviations of the Gaussian distributions were 25% of the true value. Mean ADC values calculated for each case were 0.72, 0.77, 0.76, 0.79, and $0.77 \times 10^{-3} \text{ mm}^2 \times \text{s}^{-1}$ compared with the real value, $0.76 \times 10^{-3} \text{ mm}^2 \times \text{s}^{-1}$. Relative ADC-to-noise values for the five cases were 1, 0.72, 0.88, 0.73, and 0.58. The accuracy of the method is therefore relatively immune to error in T_1 , T_2 , and M_0 ; however, with 25% error added to all parameters the precision of the method decreases $\sim 40\%$. A more complete investigation is required to determine the imaging parameters which minimize this precision loss.

The spatial resolution of traditional diffusion-weighted EPI images, and therefore of the resulting D maps, is limited in part by T_2 decay during the EPI readout. High b-value ($>1000 \text{ s} \times \text{mm}^{-2}$) dwEPI acquisitions require large gradients ($\sim 40 \text{ mT} \times \text{m}^{-1}$) applied over relatively long durations ($>17 \text{ ms}$) with significant time delay between gradients ($>40 \text{ ms}$) giving a final echo time in the range of 100 ms. Consequently, much of the measurable signal has decayed before signal readout is begun and so diffusion-weighted images are typically acquired at low resolution: 2 to 2.5 mm^3 isotropic voxels or larger. Diffusion-weighted SSFP does not require long echo times and thus T_2 -related decay does not limit the spatial resolution of the acquired images. The high diffusion sensitivity of diffusion-weighted SSFP allows for the collection of strongly diffu-

sion-weighted images with modest gradient strengths and significantly shorter gradient durations compared with pulsed-gradient spin-echo-based methods. This has been previously reported in Refs. 7 and 8.

The high diffusion sensitivity of dwSSFP makes the sequence extremely sensitive to bulk patient motion, such as that related to cardiac and respiratory motion. In our initial in vivo neuroimaging experiences, the use of cardiac gating and breathholding reduced the appearance of these artifacts but did not eliminate them completely. Motion correction with navigator echoes has previously been shown to significantly decrease the appearance of cardiac and respiratory-related artifacts in dwSSFP images (14). Further work is required to determine the exact cause of these motion artifacts and to evaluate the necessity, effectiveness and practicality of more complex, nonlinear motion correction schemes. We believe that with adequate motion correction the DESPOD method will represent a useful new tool for quantitative diffusion mapping in vivo.

APPENDIX

Starting from Eq. [3], we multiply through by $(r-Fs)$, substitute F with $K\text{-sqrt}(K^2-1)$, and square both sides to get:

$$\beta^2 r^2 + 2\beta r E_2 A - 2\beta r K - 2\beta^2 r s K + E_2^2 A^2 - 2E_2 A K - 2E_2 A \beta s K + 1 + 2\beta s + \beta^2 s^2 = 0. \quad [\text{A1}]$$

Next, we can collect the k terms and simplify Eq. [A1] to:

$$\beta^2 r^2 + 2\beta r E_2 A + E_2^2 A^2 + 1 + 2\beta s + \beta^2 s^2 = K(2\beta r + 2\beta^2 r s + 2E_2 A + 2E_2 A \beta s) \quad [\text{A2}]$$

which we can break into three parts for simplicity: Part I = $\beta^2 r^2 + 2\beta r E_2 A + E_2^2 A^2 + 1 + 2\beta s + \beta^2 s^2$, Part II = K , Part III = $2\beta r + 2\beta^2 r s + 2E_2 A + 2E_2 A \beta s$.

Expanding each part and collecting the A terms yields the following polynomials. Starting with Part I:

$$aA^2 + bA + c, \quad [\text{A3a}]$$

where

$$a = \beta^2 E_2^4 \cos^2 \alpha - 2\beta^2 E_1 E_2^3 \cos \alpha + \beta^2 E_1^2 E_2^4 + 2\beta E_2^3 \cos \alpha - 2\beta E_1 E_2^2 + E_2^2 + \beta^2 E_2^2 - 2\beta^2 E_1 E_2^2 \cos \alpha + \beta^2 E_1^2 E_2^2 \cos^2 \alpha, \quad [\text{A3b}]$$

$$b = 4\beta^2 E_2^2 \cos \alpha - 4\beta E_1 E_2 \cos \alpha + 4\beta^2 E_1^2 E_2^2 \cos \alpha - 4\beta^2 E_1 E_2^2 + 4\beta E_2 - 4\beta E_1 E_2^2 \cos^2 \alpha, \quad [\text{A3c}]$$

and

$$c = \beta^2 - 2\beta^2 E_1 \cos \alpha + \beta^2 E_1^2 \cos^2 \alpha + 1 + 2\beta E_2 \cos \alpha - 2\beta E_1 E_2 + \beta^2 E_2^2 \cos^2 \alpha - 2\beta^2 E_1 E_2^2 \cos \alpha + \beta^2 E_1^2 E_2^2. \quad [\text{A3d}]$$

Likewise, from Parts II and III we obtain the following polynomials in A :

$$\frac{gA^3 + hA^2 + iA + 1}{jA^2 + kA} \quad [\text{A4a}]$$

with

$$g = -E_1E_2^2, \quad [\text{A4b}]$$

$$h = E_2^2\cos \alpha, \quad [\text{A4c}]$$

$$i = -E_1\cos \alpha, \quad [\text{A4d}]$$

$$j = -E_1E_2\cos \alpha - E_1E_2, \quad [\text{A4e}]$$

$$k = E_2\cos \alpha + E_2, \quad [\text{A4f}]$$

and

$$dA^2 + eA + f, \quad [\text{A5a}]$$

where

$$d = 2\beta^2E_2^3\cos \alpha - 2\beta^2E_1E_2^3\cos^2\alpha - 2\beta E_1E_2^3 + 2\beta^2\beta^2E_1^2E_2^3 + 2\beta E_2^2 - 2\beta E_1E_2\cos \alpha, \quad [\text{A5b}]$$

$$e = 2\beta^2E_2 - 4\beta E_1E_2^2 + 2\beta^2E_1^2E_2\cos^2\alpha - 4\beta^2E_1E_2\cos \alpha + 4\beta^2E_2^2\cos \alpha + 2\beta^2E_2^3\cos^2\alpha - 4\beta^2E_1E_2^3\cos \alpha + 2\beta^2E_1^2E_2^3 + 2E_2, \quad [\text{A5c}]$$

and

$$f = 2\beta - 2\beta E_1\cos \alpha + 2\beta^2E_2\cos \alpha - 2\beta^2E_1E_2 - 2\beta^2E_1E_2\cos^2\alpha + 2\beta^2E_1^2E_2\cos^2\alpha. \quad [\text{A5d}]$$

REFERENCES

1. Moseley ME, Kucharczyk J, Mintorovitch J, Cohen Y, Kurhanewicz J, Derugin N, Asgari H, Norman D. Diffusion weighted MR imaging of acute stroke: correlation with T2-weighted and magnetic susceptibility-enhanced MR imaging in cats. *Am J Neuro* 1990;11:423-429.
2. Chien D, Kwong KK, Gress DR, Bunanno FS, Rosen BR. MR diffusion imaging of cerebral infarction in humans. *Am J Neurol* 1992;13:1097-1102.
3. Knowles A, Piels P, Oyen R, van Kecke P. Evaluation of high resolution diffusion weighted imaging in the prostate at 1.5T and 3T. In: *Proc Tenth Annual Meeting ISMRM, Honolulu, 2002*. p 1898.
4. Matoba M, Tonami H, Yokota H, Kuginuki M, Yamamoto I. Diffusion weighted MRI for lung cancer using SPLICE sequence. In: *Proc Tenth Annual Meeting ISMRM, 2002*. p 2063.
5. Filippi M, Cercignani M, Inglesse M, Horsfield MA, Comi G. Diffusion tensor magnetic resonance imaging in multiple sclerosis. *Neurology* 2001;56:304-311.
6. Kaiser R, Bartholdi E, Ernst RR. Diffusion and field-gradient effects in NMR Fourier spectroscopy. *J Chem Phys* 1974;60:2966-2979.
7. Wu EX, Buxton RB. Effect of diffusion on the steady-state magnetization with pulsed field gradients. *J Magn Reson* 1990;90:243-253.
8. LeBihan D, Turner R, Macfall JR. Effects of incoherent motions (IVIM) in steady-state free precession (SSFP) imaging: application to molecular diffusion Imaging. *Magn Reson Med* 1989;10:324-337.
9. Carney CE, Wong STS, Patz S. Analytical solution and verification of diffusion effect in SSFP. *Magn Reson Med* 1991;19:240-246.
10. Merboldt KD, Bruhn H, Frahm J, Gyngell ML, Hanicke W, Deimling M. MRI of diffusion in the human brain: new results using a modified CE-FAST sequence. *Magn Reson Med* 1989;9:423-429.
11. Deoni SCL, Rutt BK, Peters TM. Rapid combined T1 and T2 mapping using gradient recalled acquisition in the steady-state. *Magn Reson Med* 2003;49:515-526.
12. Stehling MK, Nitz W, Holzknacht N. Fast and ultra-fast magnetic resonance tomography. Basic principles, pulse sequences and special properties. *Radiologe* 1995;35:879-893.
13. Gong J, Hornak JP. A fast T1 algorithm. *Magn Reson Imag* 1992;10:623-626.
14. Bosak E, Harvey PR. Navigator motion correction of diffusion weighted SSFP imaging. *MAGMA* 2001;12:167-176.